



ELSEVIER

Infrared Physics & Technology 38 (1997) 337–355

INFRARED PHYSICS
& TECHNOLOGY

Theoretical study of the properties of a modulated fast-flow CO₂ laser

D. Toebaert^{a,*}, P. Muys^b, E. Desoppere^a

^a Department of Applied Physics, University of Gent, Rozier 44, B-9000 Gent, Belgium

^b Radius Engineering NV, Meersstraat 138E, B-9000 Gent, Belgium

Received 7 October 1996

Abstract

The dynamic behaviour of a CO₂ laser subject to modulation of its operational parameters is studied using an internally consistent formulation of the well-known reservoir equations [K. Smith, R.M. Thomson, Computer modeling for gas lasers, Plenum, New York, 1978]. The use of practically inaccessible physical quantities is avoided leading to a transparent set of equations describing the main properties of the temporal behaviour of the laser. The model is then applied to a variety of operational modes of the laser ranging from CW lasing to cavity dumping using a resonant reflector. In all these cases, and despite the simplifications made to render the problem tractable for desktop computation, realistic results are obtained for such practically relevant quantities as electro-optic conversion efficiency (CW), peak power (*Q*-switched), pulse repetition rate and duty cycle limitations (electrically pulsed) among others. This leads us to believe that the formulation of the equations given — based on extensive experimental and theoretical experience summarised in [S. Sazhin, P. Wild, C. Leys, D. Toebaert, E. Sazhina, J. Phys. D 26 (1993) 1872–1883; S. Sazhin, P. Wild, E. Sazhina, M. Makhlof, C. Leys, D. Toebaert, J. Phys. D 27 (1994) 464–469; M. Spiridonov, C. Leys, D. Toebaert, S. Sazhin, E. Desoppere, P. Wild, S.M.P. McKenna-Lawlor, J. Phys. D 27 (1994) 962–969; D. Toebaert, P. Muys, E. Desoppere, IEEE J. Quantum Electron. 31 (10) (1995) 1774–1778; D. Toebaert, P. Muys, E. Desoppere, J. Phys. D 29 (7) (1996) 1910–1916.] — grasps the overall kinetics of the molecular discharge and can be reliably used to at least predict upper limits to the laser's performance. © 1997 Elsevier Science B.V.

PACS: 42.55.L

Keywords: CO₂ lasers; Laser modelling; Laser modulation; Laser rate equations

1. Introduction

The aim of this paper is to construct a self-contained set of differential equations describing the energy transfer processes occurring in the active medium of a fast-flow CO₂ laser. This problem has been tackled already in a variety of publications (e.g. [7–10]), covering a range of sophistication from simple four-level

* Corresponding author. Current address: HACO NV, Raketstraat 11B, B-9000 Gent, Belgium. E-mail: david.toebaert@rug.ac.be.

schemes to full-blown three-dimensional computations [3] of the vibrational energy distribution in the turbulent flow of a DC-excited fast-axial-flow $\text{CO}_2/\text{N}_2/\text{He}$ discharge (without laser action).

Up till now the evolution has been toward more and more complicated models (2D, 3D, including minority species created in the discharge, self-consistently calculating the ruling reduced electric field strength, ...), requiring the use of increasingly more powerful workstations (and/or computing time) and rendering it impractical for conducting 'computer experiments'.

Presently we reformulate the governing equations in their simplest, spatially uniform shape. The basic quantities involved are seven energy densities (J/m^3) for the translational energy (E_T), the rotational energy (E_R), the symmetric stretch mode energy (E_1), the bending mode energy (E_2), the asymmetric stretch mode energy (E_3), the nitrogen vibrational energy (E_4) and the photon energy (E_ν) respectively. No attempt is made to relate the vibrational energy densities to vibrational temperatures since it is known [11,12] that the Boltzmann distribution is inadequate in the strongly non-equilibrium conditions of the fast-axial-flow laser, and the Treanor distribution [13,14] is inappropriate for a reservoir-type model. The energy densities are then related to one another with the appropriate rate equations, with a special emphasis on the use of directly available input parameters and self-consistency: the resulting set of equations, when summed, should produce an overall energy balance ensuring no net 'leakage' of energy into or out of the system. The latter may seem self-evident but can be a problem if different terms in the equations are derived from different physical reasonings, producing a model that in principle is self-contained, but fails to have this property when all quantities are numerically substituted into the equations. The good results obtained with the present model, in spite of all simplifications, is to our opinion due to this strict 'book-keeping'.

In Section 2 we describe in short the derivation of the equations, highlighting specific changes compared to former formulations. The overall energy balance is put forward and discussed. Section 3 then applies the model to a variety of operational modes of the laser. The CW start-up phenomenon is calculated in Section 3.1, together with the influence of the number of rotational sublevels instantaneously coupled to the upper laser level. The influence of the switching frequency of the switched-mode power supplies is described in Section 3.2 using Bode diagrams and a criterion for the maximum allowable switching amplitude is formulated. The linearised analysis of relaxation oscillations due to Siegman [15] is applied to the laser response to a small perturbation of the cavity Q factor (Section 3.3). Electrically pulsed operation is studied as a function of pulsing frequency in Section 3.4, and limitations on the duty-cycle are derived. Section 3.5 applies the standard Rigrod analysis to the results of a computer experiment calculating the laser power versus output coupler reflectivity characteristic. Section 3.6 then studies the Q -switching behaviour of the laser by simulating a rotating chopper wheel and a resonant Fabry–Pérot etalon. Finally the use of such an etalon as a piezoelectrically driven cavity dump is discussed in Section 3.7 on the basis of the calculated responses of the laser. Section 4 draws some conclusions on the use of the presented model for laser engineering and quick assessment of the influence of various operational parameters on the performance of the laser.

2. The model

2.1. Definition of the energy densities

The physical situation is modelled as a problem of interacting energy reservoirs, each interaction being described by an appropriate time constant which itself may be a function of the instantaneous configuration of the system, giving rise to non-linear behaviour. From the start it should be emphasised that the system is 'heavily damped' due to the outcoupling of laser power and the rapid relaxation to the translational degrees of freedom. So the resulting equations will be written in an essentially linear form, all non-linearity induced by the dependence of the relaxation rates on the system configuration indicated by superscripts to the symbols used (see Section 2.3).

The translational energy density E_T can be related to the gas temperature T (K) by definition of the heat capacity at constant pressure c_p (J/kg K):

$$E_T = \rho(T_{\text{ref}})h_{\text{ref}} + \int_{T_{\text{ref}}}^T \rho(T)c_p(T)dT \quad (1)$$

where ρ (kg/m³) is the mass density of the mixture and h (J/kg) is the specific enthalpy. Taking the reference temperature to be T_0 , the gas inlet temperature, neglecting the temperature dependence of the heat capacity in the temperature range $T_0 < T < 600$ and using the ideal gas law leads to the particularly straightforward relation between E_T and T :

$$E_T = \frac{pc_p}{R} \ln\left(\frac{T}{T_0}\right) \quad (2)$$

where p (Pa) is the operational pressure and R (J/kg K) the specific gas constant of the mixture.

The rotational energy density E_R is assumed to be in equilibrium with the translational degrees of freedom. Even for the highest rotational level experimentally detected [4], the $J = 92$ level of the vibrational ground state $|00^0_0\rangle$, the energy gap to the $J = 93$ level is only 9 meV, which is to be compared to $kT_0 \approx 25$ meV. The rotational relaxation time is thus basically the average time between molecular collisions, which can be estimated from the gas density N (m⁻³), elastic collision cross section σ (m²) and the average thermal velocity $\langle v \rangle$ (m/s) to be

$$\langle \tau_c \rangle = \frac{1}{N\sigma\langle v \rangle} \approx 0.1 \text{ ns} \times \frac{10^5}{p(\text{Pa})} \quad (3)$$

using the equipartition law and $\sigma \approx 10^{-18}$ m² [1]. On time scales larger than $\langle \tau_c \rangle$ the difference between rotational and translational temperature is quite negligible. In what follows we will use $E_{\text{TR}} = E_T + E_R$ for brevity.

The vibrational energy density in a particular mode E_i ($i = 1, 2, 3, 4$) is obtained by summation over a Treanor distribution of level populations:

$$E_i = \sum_{\lambda=0}^{\infty} N_{\lambda} [\lambda - \lambda(\lambda - 1)x^*] G = \sum_{\lambda=0}^{\infty} N_0 [\lambda - \lambda(\lambda - 1)x^*] G \exp[-(\lambda G/T_v^* - \lambda(\lambda - 1)Gx^*/T)/k] \quad (4)$$

introducing the term value G , i.e. the energy of the first excited level of the mode ($\lambda = 1$), most conveniently expressed in cm⁻¹ (note that Boltzmann's constant evaluates to $k \approx 0.695$ cm⁻¹/K). The dimensionless factor x^* (referred to G) is the *anharmonicity factor* and causes the observed deviation from a Boltzmann distribution. The parameter T_v^* (K) is referred to as the Treanor vibrational temperature.

The photon energy density E_{ν} is related to the (assumed monochromatic) intra-cavity radiation intensity I_{ν} (W/m²) by

$$E_{\nu} = \frac{I_{\nu}}{c} = \frac{1}{2} \epsilon_0 \frac{A^2 + B^2}{2} \quad (5)$$

if A and B (V/m) are the amplitudes of the right- and left-running waves that make up the standing wave in the Fabry–Pérot type cavity. Eq. (5) averages the electric field in time over a period $1/\nu$ and in space over a wavelength λ .

2.2. Time evolution of the energy densities

The power input into the discharge is initially distributed over the various degrees of freedom of the gas depending on the electron energy distribution function (EEDF) $f(\epsilon)$ (eV^{-3/2}), where ϵ is the electron energy

expressed in eV. The EEDF is calculated using the widespread Boltzmann solver ELENDIF [16], with excitation cross sections taken from [17] and updated where appropriate with the data from [18]. The code is fed with experimental values for the reduced electric field strength [19] (which is the single most important parameter determining the EEDF), and takes into account the influence of superelastic collisions on the shape of the distribution. The latter cannot be ignored due to significant population buildup in the excited vibrational levels. The rovibrational temperatures specified in the input data for ELENDIF are again taken from experiment [6]. From the output of ELENDIF the fractions χ_i of input power supplied to the various E_i , ($i = T, R, 1, 2, 3, 4$) are directly available and obey $\sum_i \chi_i = 1 - \chi_{el}$, where χ_{el} is the fraction of energy spent on the electronic processes occurring in the discharge (electronic excitation, ionisation, ...).

The V–TR and V–V' relaxation processes are described by Landau–Teller equations [1] of the general form

$$\frac{\partial E_i}{\partial t} = - \frac{E_i - E_i^{(T, T_j, \dots)}}{\tau^{(T, T_j, \dots)}} \quad (6)$$

where the superscripts denote the dependence of the 'quasi-equilibrium' values and the relaxation rates on the instantaneous configuration of the system. Inherent to the derivation of Eq. (6) is the assumption of harmonic oscillator interaction. As an example illustrating Eq. (6) one can find for the interaction between two non-degenerate harmonic oscillator modes L and M :

$$E_L^{(T, T_M)} = NG_L \frac{1}{\exp[G_M/kT_M] \exp[(G_L - G_M)/kT] - 1} \quad (7)$$

and

$$\frac{1}{\tau^{(T, T_M)}} = Nk_{1,0;0,1} \frac{\exp[(G_M - G_L)/kT] \{ \exp[G_M/kT_M - (G_M - G_L)/kT] - 1 \}}{\exp[G_M/kT_M] - 1} \quad (8)$$

showing the dependence of the 'quasi-equilibrium' value to which the vibrational energy E_L relaxes and the associated time constant on the vibrational temperature of the other mode, and on the gas temperature if the process is non-resonant ($G_L \neq G_M$). $k_{1,0;0,1}$ (m^3/s) is the (temperature dependent) rate constant of the process where a quantum of the first excited level of the L mode is transferred to the M mode (this process can have a positive or negative energy defect). To calculate $E^{(T, T_j, \dots)}$ we use, by lack of alternative, the Boltzmann distribution obtained from Eq. (4) by putting $x^* = 0$. In any case this is a far better approximation than putting $E^{(T, T_j, \dots)} \equiv ct$, which would lead to a purely exponential relaxation. As to the relaxation rate $\tau^{(T, T_j, \dots)}$, it should be noted that the formulas used (taken from [2], who give the results of [1] with some minor corrections) are in fact fits to experimental data [20], and as such are essentially correct.

Coupling to the laser field is described by the 'field–matter coupling constant' (Einstein A -coefficient) $A = 1/\tau_{sp}$ (Hz) as

$$\frac{\partial E_\nu}{\partial t} = cE_\nu S_{|\rangle} g(\nu - \nu_0) + \varphi h\nu N_{|+1\rangle} A_{|+1\rangle} - \frac{E_\nu}{\tau_c} \quad (9)$$

where we introduce the intensity of the transition $S_{|\rangle}$ (m^{-1} Hz, or, more commonly used, cm^{-2}):

$$S_{|\rangle} = \frac{\lambda^2}{8\pi} A_{|+1\rangle} \left(N_{|+1\rangle} - \frac{g_{|+1\rangle}}{g_{|\rangle}} N_{|\rangle} \right) = \frac{\lambda^2}{8\pi} A_{|+1\rangle} \Delta N. \quad (10)$$

The subscripts $|\rangle$ and $|+1\rangle$ are shorthand for lower and upper laser level. The line shape function $g(\nu - \nu_0)$ (Hz^{-1}) is in general a Voigt profile and should be evaluated at the cavity resonant frequency ν . In the simplest case we can assume the transition to be predominantly pressure broadened and evaluate the resulting Lorentz

line shape at line centre: $g(0) \approx 2/\pi\Delta\nu_L$. The value of the pressure-broadened linewidth is calculated from the Stern–Vollmer expression [21]:

$$\Delta\nu_L = 7.58(\chi_{\text{CO}_2} + 0.73\chi_{\text{N}_2} + 0.64\chi_{\text{He}})p\sqrt{\frac{300}{T}} \quad (11)$$

where T is in Kelvin, p in Torr and the result is in MHz. The cavity decay rate, related to the cavity Q -factor by $Q = 2\pi\nu\tau_c$, can be written as

$$\frac{1}{\tau_c} = \sum_m \frac{1}{\tau_m} = \frac{1}{\tau_r} \sum_m \ln \frac{1}{1 - \mathcal{L}_m} \quad (12)$$

where τ_r is the cavity round-trip time and \mathcal{L}_m is the fractional intensity loss per round trip due to loss process m (output coupling, diffraction losses, ...). φ is the fraction of spontaneous emission along the resonator axis, which can be estimated from geometrical considerations [1].

Cooling of the gas is described by its time constant τ_d , which for a fast-flow laser is the transit time of the gas through the discharge. For our experimental laser this can be estimated from the pump volume flux to be approximately 1.2 ms. The term to be added to all equations (except for E_ν) is then written as

$$\frac{\partial E_i}{\partial t} = - \frac{E_i - E_i^{(T_0, T_0, \dots)}}{\tau_d} \quad (13)$$

assuming perfect heat exchangers.

2.3. Resulting equations and energy balance

The results are summarised in the following 6×6 set of first-order non-linear differential equations:

$$\begin{aligned} \frac{\partial E_{\text{TR}}}{\partial t} &= (\chi_T + \chi_R)P_{\text{in}} + \frac{E_1 - E_1^{(T)}}{\tau_{10}^{(T)}} + \frac{E_2 - E_2^{(T)}}{\tau_{20}^{(T)}} + \left(1 - \frac{G_1}{G_3} - \frac{G_2}{G_3}\right) \frac{E_3 - E_3^{(T, T_1, T_2)}}{\tau_3^{(T, T_1, T_2)}} \\ &\quad - \frac{(E_T + E_R) - (E_T^{(T_0)} + E_R^{(T_0)})}{\tau_d} + (e_R(20) - e_R(19)) \left(\frac{N_{|00^0 1; 19\rangle}}{\tau_{\text{sp}}} + W\Delta N \right), \\ \frac{\partial E_1}{\partial t} &= \chi_1 P_{\text{in}} - \frac{E_1 - E_1^{(T)}}{\tau_{10}^{(T)}} + G_1 \left(\frac{N_{|00^0 1; 19\rangle}}{\tau_{\text{sp}}} + W\Delta N \right) - \frac{E_1 - E_1^{(T_2)}}{\tau_{12}^{(T, T_2)}} - \frac{E_1 - E_1^{(T_0)}}{\tau_d} + \frac{G_1}{G_3} \frac{E_3 - E_3^{(T, T_1, T_2)}}{\tau_3^{(T, T_1, T_2)}}, \\ \frac{\partial E_2}{\partial t} &= \chi_2 P_{\text{in}} - \frac{E_2 - E_2^{(T)}}{\tau_{20}^{(T)}} + \frac{E_1 - E_1^{(T_2)}}{\tau_{12}^{(T, T_2)}} - \frac{E_2 - E_2^{(T_0)}}{\tau_d} + \frac{G_2}{G_3} \frac{E_3 - E_3^{(T, T_1, T_2)}}{\tau_3^{(T, T_1, T_2)}}, \\ \frac{\partial E_3}{\partial t} &= \chi_3 P_{\text{in}} + \frac{E_4 - E_4^{(T_3)}}{\tau_{43}^{(T)}} - \frac{E_3 - E_3^{(T, T_1, T_2)}}{\tau_3^{(T, T_1, T_2)}} - G_3 \left(\frac{N_{|00^0 1; 19\rangle}}{\tau_{\text{sp}}} + W\Delta N \right) - \frac{E_3 - E_3^{(T_0)}}{\tau_d}, \\ \frac{\partial E_4}{\partial t} &= \chi_4 P_{\text{in}} - \frac{E_4 - E_4^{(T_3)}}{\tau_{43}^{(T)}} - \frac{E_4 - E_4^{(T_0)}}{\tau_d}, \\ \frac{\partial E_\nu}{\partial t} &= - \frac{E_\nu}{\tau_c} + h\nu \left(\varphi \frac{N_{|00^0 1; 19\rangle}}{\tau_{\text{sp}}} + W\Delta N \right) \end{aligned} \quad (14)$$

introducing the stimulated emission probability $W = (c/h\nu)(\lambda^2/8\pi)A_{|+1\rangle} E_\nu g(\nu - \nu_0)$ (Hz).

Defining the total energy density as

$$E = E_{\text{TR}} + \sum_{i=1}^4 E_i + E_\nu = \tilde{E} + E_\nu \quad (15)$$

and summing (Eq. (14)), taking into account that $h\nu = [G_3 + e_R(19)] - [G_1 + e_R(20)]$, where $E_R(J)$ is the energy of the J th rotational sublevel, leads to

$$\frac{\partial E}{\partial t} = (1 - \chi_{\text{el}}) P_{\text{in}} - \frac{\tilde{E} - \tilde{E}^{(T_0)}}{\tau_d} - \frac{E_\nu}{\tau_c} - h\nu(1 - \varphi) A_{|00^0_1;19\rangle} N_{|00^0_1;19\rangle} \quad (16)$$

In steady state we obtain an ‘external’ energy balance revealing the main energy flows:

$$P_{\text{in}} = \chi_{\text{el}} P_{\text{in}} + \frac{\tilde{E} - \tilde{E}^{(T_0)}}{\tau_d} + \frac{E_\nu}{\tau_c} + h\nu(1 - \varphi) A_{|+1\rangle} N_{|+1\rangle} \quad (17)$$

This last equation simply states that the power coupled into the discharge must compensate for the electronic processes, is partly removed as waste heat, is partly coupled out as useful laser power and/or lost as diffracted and scattered radiation, and is partly radiated out of the discharge as spontaneous emission.

The non-linearity of the model has two distinct causes: the stimulated emission term and the ‘{ }’ superscripts. The latter form the main distinction with level-type approaches for laser calculations, which substitute $\{T, T_m\} \rightarrow \{T, T\}$ or even $\{T, T_m\} \rightarrow \{T_0, T_0\}$ in (Eq. (14)). For molecular lasers, in particular CW, this substitution cannot be justified since these lasers operate on relatively low-lying levels and as such are very sensitive to thermal effects.

3. Application of the model

3.1. CW start-up phenomenon

Fig. 1 shows the transient behaviour when the laser is initially turned on (‘cold start’). The delay time before the gain spike is approximately 60 μs and is due to the time it takes for the nitrogen vibrational mode to accumulate the excitation energy, followed by the subsequent relaxation to the CO_2 asymmetrical stretch mode. The gain spike is damped out after a few tens of microseconds after which the output power closely follows the

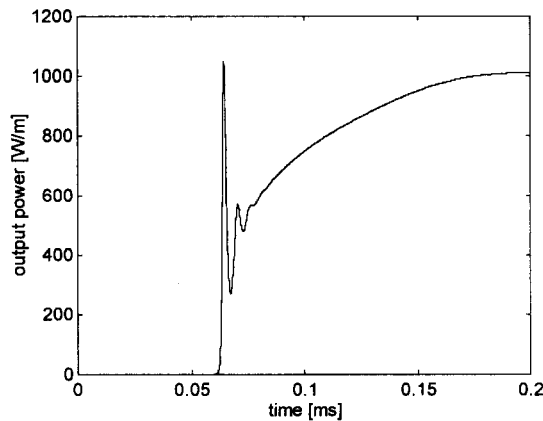


Fig. 1. Transient start-up phenomenon. The CW power level of about 1 kW/m is reached after a few times the discharge transit time.

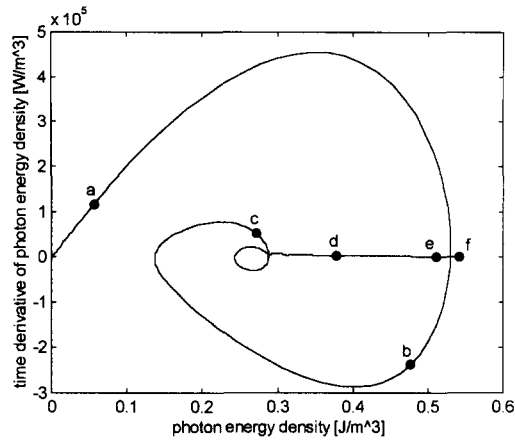


Fig. 2. Phase plot of the intra-cavity photon density E_p . The time marks a to f are at 63, 65, 70, 100, 200 and 1000 μs .

electrical pulse shape (to calculate the start-up behaviour the current pulse frequency was set to 50 Hz). The higher frequency harmonics of the pulsing frequency are filtered out by the buffer-like action of the pumping gas. Only the fraction of the input energy coupled directly into the CO_2 asymmetric stretch mode ($\approx 1\%$) causes instantaneous fluctuations of the output power which are too small to be visible in Fig. 1.

A phase plot of the intra-cavity photon energy density (Fig. 2) reveals the existence of a quasi-equilibrium value circled by the trajectory (part a, b, c, d of the trace) before settling to its final equilibrium value (point f). The former is determined by the gain seen by the initial gain spike (low E_3 and low T), the latter by the equilibrium energy distribution (high E_3 , increased T). Finally Fig. 3 shows the evolution of the gas temperature. The long-term behaviour is clearly dominated by the gas residence time τ_d . The inset shows the increased heating rate due to the onset of lasing at $t \approx 60 \mu\text{s}$. Depending on the ratio of the residence time to the net VT relaxation rate, this will lead to an increased or decreased equilibrium temperature. In the modelled situation, as in all practical fast-axial-flow lasers with $p \approx 100 \text{ mbar}$ and $\tau_d \approx 1 \text{ ms}$, the steady-state temperature is lower when lasing [6].

Depending on the ratio of the rotational intra-mode relaxation time τ_{RR} to the cavity round-trip time τ_r , the transient start-up spike will look differently. In the previous calculations, as well as in the following paragraphs, the number of rotational levels \mathcal{N}_J contributing to the upper laser level population [22] by RR relaxation within

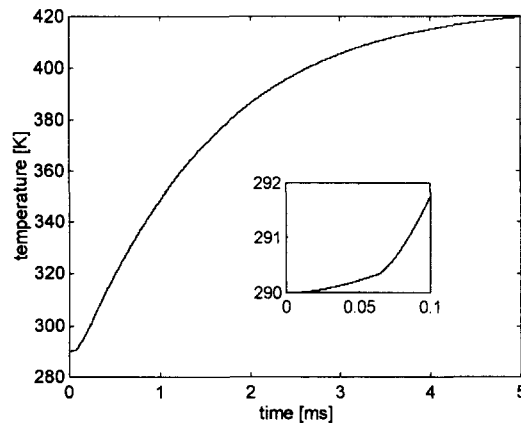


Fig. 3. Time evolution of the gas temperature. The inset shows the increased heating rate when the laser field starts to develop.

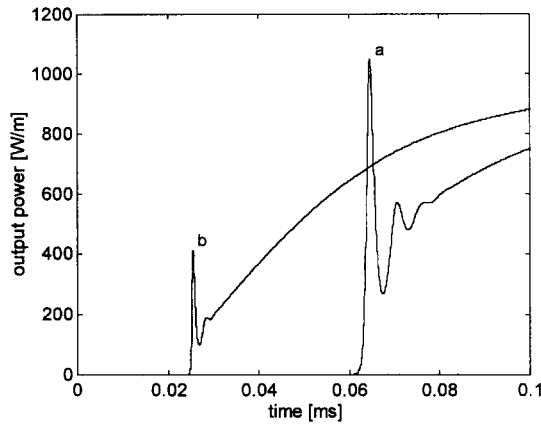


Fig. 4. Influence of the number of rotational sublevels instantaneously coupled to the laser field. (a) $\mathcal{N}_J = 1$, (b) $\mathcal{N}_J = \infty$.

the cavity round trip time, will always be set to unity. This means that we only consider the populations of the particular rovibrational levels involved in the laser action (single-line P20 operation assumed throughout). Fig. 4 shows the effect of assuming the opposite, $\mathcal{N}_J = \infty$ ($\tau_{RR} = 0$). Due to the higher instantaneous gain as seen by the developing laser field, the delay time is shorter (the threshold inversion is reached earlier), but the extent in which the population inversion grows beyond the threshold value is lower, resulting in a weaker transient. In reality we have $1 < \mathcal{N}_J < \infty$ and the transient will lie between the extremes shown in Fig. 4 [22].

3.2. Short-term, input power induced, output power fluctuations

The switched-mode all-solid-state high-voltage power supply used in the experimental laser [4–6] has a switching ripple on the output current with a relative amplitude ξ_{in} of approximately 5% of the DC value of the current and a frequency $f_s = 50$ kHz. A period $\tau_s = 20$ μ s consists of an exponentially rising flank (charging the capacitors) followed by an exponentially decaying one (discharge of the capacitors after switching).

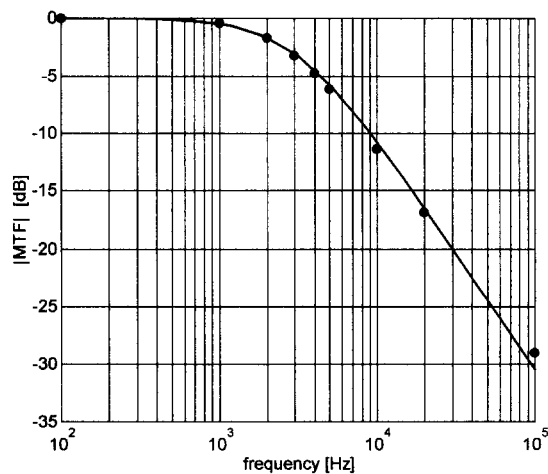


Fig. 5. Magnitude of the MTF as a function of frequency. The solid line is the Bode diagram for a first order system with a 3 dB cutoff frequency of 3 kHz.

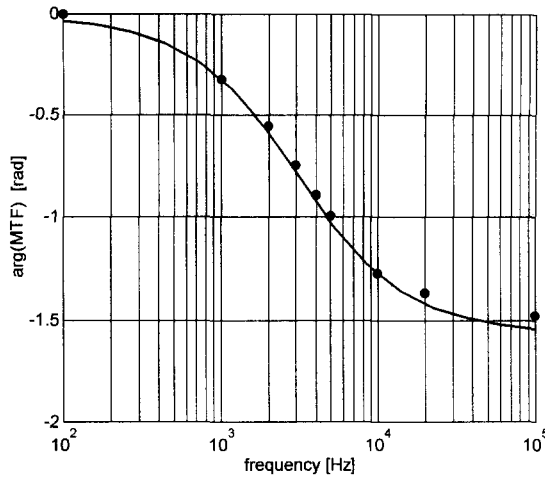


Fig. 6. Phase retardation of the MTF as a function of frequency. The solid line is the phase diagram of the same system as in Fig. 5.

To study the influence of the switching frequency of the high-voltage supply on the short term fluctuations of the laser output we determine the ‘modulation transfer function’ in the frequency range 100 Hz–100 kHz:

$$\text{MTF}(\omega) = \frac{\Delta E_\nu(\omega)/E_\nu^{\text{DC}}}{\Delta P_{\text{in}}(\omega)/P_{\text{in}}^{\text{DC}}} = \frac{\xi_\nu \exp(j\varphi_\nu)}{\xi_{\text{in}}} \quad (18)$$

where we have introduced the angular frequency ω (rad s⁻¹) for the electrical frequency to avoid confusion with the laser frequency ν . The $\exp(j\omega t)$ dependence cancels out in regime and $\varphi_\nu = \arg(\Delta E_\nu(\omega)) - \arg(\Delta P_{\text{in}}(\omega))$ is the response’s phase shift. Figs. 5 and 6 show the amplitude and phase diagram of the MTF. The solid curves are the Bode diagrams for a first order system, $\text{MTF}_1(\omega) = 1/(1 + j\omega\tau_{\text{c.o.}})$, fitted to the calculated data, yielding a 3 dB cutoff frequency $f_{\text{c.o.}} = 1/2\pi\tau_{\text{c.o.}} = 3$ kHz ($\tau_{\text{c.o.}} = 53$ μ s). To limit the influence of the switching component of the electric power on the laser output to a maximum value of ξ_ν^{max} requires limiting the switching ripple to

$$\frac{\xi_{\text{in}}}{1 + (2\pi f_s \tau_{\text{c.o.}})^2} < \xi_\nu^{\text{max}} \quad (19)$$

as a function of the switching frequency. For switching frequencies greater than 10 kHz, the power output modulation is less than 0.5% for input modulation (relative) amplitudes up to 5%.

3.3. Relaxation oscillations

A small perturbation of the intra-cavity photon density causes the onset of relaxation oscillations to restore equilibrium. To observe this phenomenon it is necessary that the perturbation happens on a faster time scale than the smallest VT or VV relaxation rate, typically some microseconds. To model this, we introduce a small ‘dip’ in the cavity decay rate with a Gaussian shape, a peak value of 5% of the undisturbed value and a FWHM of 1 μ s. Fig. 7 shows the calculated response $\Delta E_\nu(t) = E_\nu(t) - E_\nu^{\text{DC}}$ (circles). The inset shows the perturbed cavity decay rate.

The analysis of these relaxation oscillations, for small perturbations, can be linearised. Following [15], we put

$$\Delta E_\nu = A_0 \exp\left(-\frac{t - t_0}{\tau_{\text{r.o.}}}\right) \sin(\omega_{\text{r.o.}} t + \phi) h(t - t_0) \quad (20)$$

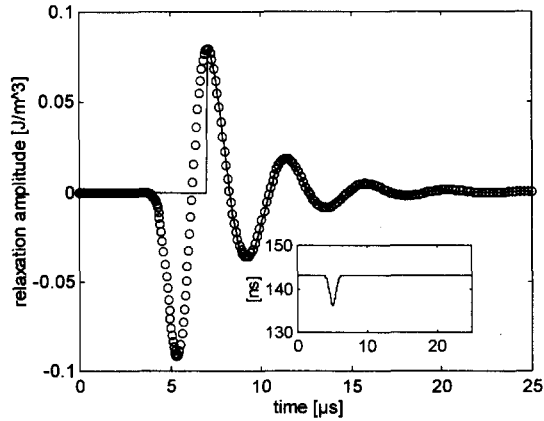


Fig. 7. Relaxation amplitude for a cavity decay time disturbed as shown in the inset. \circ : calculated; solid line: linearised analysis.

where the parameters A_0 , $\tau_{r.o.}$, $\omega_{r.o.}$ and ϕ are determined by a least squares fit (solid curve in Fig. 7) to the calculated response. The unit step function $h(t-t_0)$ is introduced to limit the fit to points where the perturbation itself is already finished. In the present case we put $t_0 = 7 \mu\text{s}$. From the fit the following values are obtained:

$$A_0 = 8.6825 \times 10^{-2} \text{ J/m}^3, \quad \tau_{r.o.} = 1/\gamma_{r.o.} = 2.9157 \mu\text{s}, \quad \omega_{r.o.} = 1.4478 \text{ MHz}, \quad \phi = -5.2379 \quad (21)$$

From these parameters we can calculate the normalized pump parameter r and the effective decay rate of the upper laser level γ_2 (we follow the notations of [15], p. 962):

$$r = \frac{2\gamma_{r.o.}\gamma_c}{2\gamma_{r.o.}\gamma_c - (\omega_{r.o.}^2 + \gamma_{r.o.}^2)} \approx 1.87, \quad \gamma_2 = \frac{2\gamma_{r.o.}}{r} \approx 0.367 \text{ MHz} \quad (22)$$

where $\gamma_c = 1/\tau_c$. Finally we obtain the saturation intensity I_{sat} :

$$I_{\text{sat}} = \frac{h\nu}{\sigma} \gamma_2 \approx 364 \frac{\text{W}}{\text{cm}^2} \quad (23)$$

where σ is the stimulated emission cross section:

$$\sigma(\nu)\Delta N = S_{ij}g(\nu - \nu_0) \quad (24)$$

This high value for the saturation intensity is the underlying reason for the scalability of molecular gas lasers to high power, in contrast to lasers operating on electronic transitions.

3.4. Electrically pulsing the laser

Fig. 8 shows the resulting pulse train when the discharge current is pulsed at a frequency of 1 kHz, with a 50% duty-cycle. The relatively slow decay of the output power is completely due to the energy stored in the nitrogen gas. Fig. 9 zooms in on the afterglow in a semi-logarithmic plot. The straight line is a purely exponential decay with a time constant $\tau_v = 38 \mu\text{s}$. The latter is in very good agreement with the value obtained by following a vibrational quantum of energy in the afterglow:

$$\tau_{43} + \frac{1}{1/(\tau_{12} + \tau_{20}) + 1/\tau_{10}} \approx 37 \mu\text{s} \quad (25)$$

using the values of the time constants just before the power is switched off. At a pulsing frequency of 1 kHz the

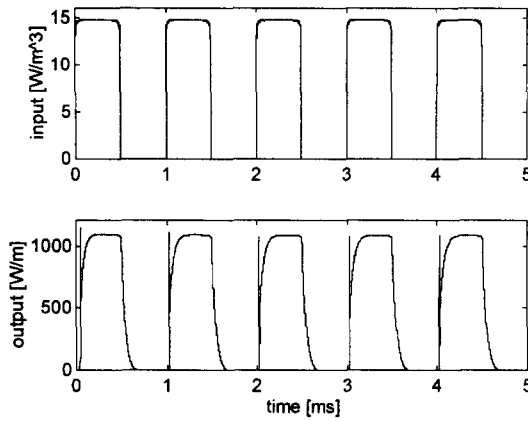


Fig. 8. Lower trace: laser output power for an electrical excitation pulse shape as shown in the upper trace.

laser extinguishes completely in between pulses, which is almost always desirable. The maximum frequency for which this still happens is given by

$$f^{\max} = -\frac{1}{\tau_v^{(\delta)} \ln \chi} \tag{26}$$

as a function of the allowable fraction χ of the maximum power present in between pulses. The superscript in $\tau_v^{(\delta)}$ indicates explicitly the dependence of the time constant on the duty cycle (through the system equations). For the calculated case and $\chi = 10^{-3}$ we find $f^{\max} = 3.8$ kHz. Fig. 10 shows the first millisecond of the outcoupled power for $\delta = 0.5$ and pulse frequencies between 1 and 7 kHz.

Besides the limitation on the maximum pulse frequency at fixed δ there is an analogous limitation on the duty cycle for a fixed pulse frequency:

$$\delta \leq 1 + f\tau_v^{(\delta)} \ln \chi \tag{27}$$

This implicit equation can only be used to estimate δ^{\max} for a (calculated or measured) $\tau_v^{(\delta)}$. For $f = 1$ kHz, $\chi = 10^{-3}$ and using $\tau_v^{(0.5)}$ we find $\delta^{\max} = 75\%$.

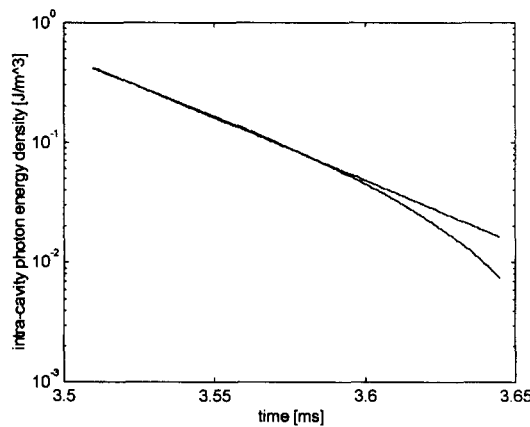


Fig. 9. Expanded view of the pulse tail. The straight line is a purely exponential fit to $E_v(t)$ for a fixed time constant of 38 μ s.

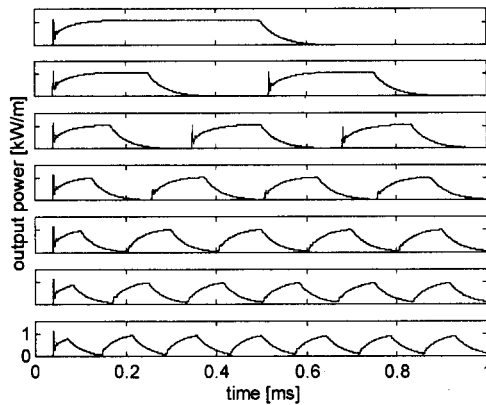


Fig. 10. Evolution of the pulse shape as a function of frequency, for a duty cycle of 50%. Top to bottom trace: pulse frequency 1 to 7 kHz.

3.5. Small-signal gain and saturation intensity: Rigrod analysis

In this paragraph we apply the analysis due to Rigrod [23], with the notations as in [15], to the results of a computer experiment where we varied the output coupling coefficient between $\mathcal{L} = 90\%$ and $\mathcal{L} = 2\%$ (see Eq. (12)). Fig. 11 shows the CW output intensity I_{out} for different output couplers. The solid line is a least squares fit to the Rigrod formula

$$I_{\text{out}} = \frac{T_2 I_{\text{sat}}}{(1 + r_2/r_1)(1 - r_1 r_2)} (\ln G_0 - \ln(1/r_1 r_2)) \quad (28)$$

where $r = \sqrt{1 - T}$ and $G_0 = \exp(2\alpha_{m0} L_m)$, with α_{m0} (m^{-1}) the amplitude small-signal gain and L_m (m) the length of the active medium. The output coupler has a power transmission T_2 , and the reflectivity r_1 is very close to unity (perfect mirror) and condenses all distributed losses. The fit does not use the extreme points $\mathcal{L} < 5\%$ because in these conditions the parasitic losses are no longer negligible compared to the extraction of laser power and the model is a too idealised picture. The fit parameters for the curve shown in Fig. 11 lead to a

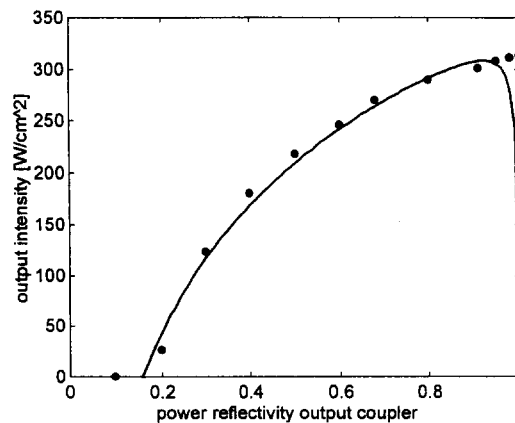


Fig. 11. CW output power as a function of the output coupler reflectivity. Solid line: Rigrod analysis excluding $R > 95\%$.

power small-signal gain coefficient $\gamma_{m0} = 2\alpha_{m0} = 1.154 \text{ m}^{-1}$ and a saturation intensity of $I_{\text{sat}} = 366 \text{ W/cm}^2$, in excellent agreement with the results obtained by the relaxation oscillation analysis.

The extraction efficiency is given by

$$\eta_{\text{extr}} \equiv \frac{I_{\text{out}}}{I_{\text{avail}}} = \frac{T_2}{(1 + r_2/r_1)(1 - r_1 r_2)} \left(1 + \frac{\ln r_2 r_1}{\ln G_0} \right) \quad (29)$$

where $I_{\text{avail}} = I_{\text{sat}} \ln G_0$ is the maximal intensity available from an active medium with characteristic parameters I_{sat} and G_0 . The extraction efficiency reaches its maximal value $\eta_{\text{extr}}^{\text{max}} = 93.6\%$ for $R_2 = r_2^2 = 94\%$. On the other hand we can say that the maximum extraction efficiency is determined by the ratio of the maximum electro-optical efficiency to the value derived from the excitation (discharge) efficiency $\eta_d = \chi_4 + \chi_3 = 71\%$ and the quantum efficiency $\eta_q = G_4/(G_3 - G_1) \approx 43\%$:

$$\eta_{\text{extr}}^{\text{max}} = \frac{\eta_{\text{e.o.}}^{\text{max}}}{\eta_d \eta_q} = 94.7\% \quad (30)$$

where we calculate the maximum electro-optical efficiency as the ratio of the maximum available power to the electrical input power:

$$\eta_{\text{e.o.}}^{\text{max}} = \frac{I_{\text{sat}} \ln G_0}{L_m P_{\text{in}}} = 28.6\% \quad (31)$$

Both values for $\eta_{\text{extr}}^{\text{max}}$ are in good agreement. Experimentally we obtained a maximal electro-optical efficiency of 26.4%, for an output coupler reflectivity $R_2 = 91\%$. The theoretical extraction efficiency derived from Eq. (29) for $R_2 = 91\%$ is 0.93. The calculated electro-optical efficiency then amounts to $\eta_{\text{e.o.}}^{\text{max}} \times \eta_{\text{extr}}(R_2 = 91\%) = 26.6\%$.

3.6. Q-switching a DC-excited fast-axial-flow CO₂ laser

3.6.1. Using a mechanical chopper

The rotating chopper wheel is simulated as a smoothed square wave time dependence of the cavity decay rate. For example a chopper wheel of diameter 10 cm, with 24 (1 mm) slits evenly spaced on the perimeter, rotating at 10000 rpm leads to a cavity ‘on’ time Δt_Q of approximately 19 μs and a pulse repetition rate $\nu_Q \approx 4 \text{ kHz}$. Fig. 12 shows the resulting sequence of Q-switched spikes. Fig. 13 zooms in on a single giant pulse to

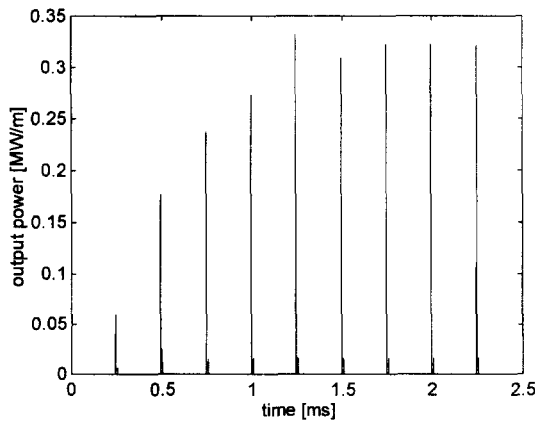


Fig. 12. 4 kHz, mechanically Q-switched pulse train (cold start).

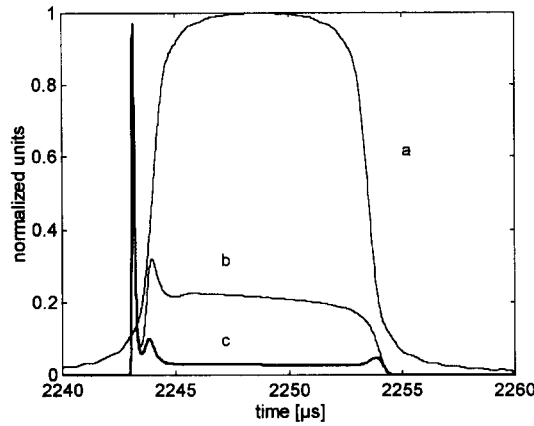


Fig. 13. (a) $\tau_c(t)$; (b) $E_v(t)$; (c) $P_{\text{out}}(t)$. All quantities are normalized to their maximum values to facilitate comparison.

show the time evolution of the cavity decay rate, the intra-cavity photon energy density and the output power. The pulse energy is given by

$$E_Q = \int_{\text{puls}} \frac{E_v(t)}{\tau_T(t)} dt \approx \sum_m^{(\text{puls})} \frac{E_v(t_m)}{\tau_T(t_m)} (t_{m+1} - t_m) \quad (32)$$

where the sum uses the discrete data obtained from the ODE-solver¹ used to solve Eq. (14), and τ_T is the part of the cavity decay time due to transmission through the output coupler (Eq. (12)). The total pulse energy reaches a stable value of approximately 650 J/m³ after the seventh pulse (0.65 mJ/cm³, meaning ‘per cm³ of active medium’). The peak power in the giant pulse is 0.335 MW/m. The average laser output power amounts to $\langle P_{\text{out}} \rangle = \nu_Q E_Q = 737$ W/m where the main contribution stems from the pulse tail. In practice one needs to compromise between peak pulse intensity and total pulse energy. Table 1 shows the results for three model calculations. The variation of pulse shape is shown in Fig. 14. The lowering of pulse energy with shorter Δt_Q is completely due to cutting the pulse tail. At high pulse repetition rates the average power increases again since the increasing frequency over-compensates the lowering of the pulse energy.

3.6.2. Using a resonant etalon

Recently [24] the use of a resonant etalon has been reported as an alternative means to obtain a modulated output from a CO₂ laser. The etalon transmission is given in terms of the incident wavelength λ , refractive index of the intermediate medium n , etalon spacing d and reflection coefficient of the inner surfaces $R(\lambda)$ (assumed equal) by:

$$T_{\text{et}} = \frac{(1 - R)^2}{1 + R^2 - 2R \cos(4\pi nd/\lambda)} \quad (33)$$

By mounting one of the optics on a piezoactuator it is possible to modulate the etalon spacing and hence the resonator Q factor. To realise Q -switching with such a device it is necessary to have a sharp transition from a transparency high enough to prevent laser oscillation to a value above threshold. Fig. 15 shows the resulting reflectivity of the etalon for a saw-tooth spacing modulation with an amplitude of 1 μm and a frequency of 100 kHz, with $R = 0.3$. The resulting rise-time of the reflectivity is approximately 3.5 μs . Fig. 16 shows the

¹ MATLAB® Ref. Guide 1992, MathWorks, Natick, MA 01760, USA and references therein.

Table 1

Mechanically Q -switched pulse characteristics. The labels in the first column refer to the labels in Fig. 14. The last column lists the peak power in the giant pulse

Pulse shape	ν_Q (kHz)	Δt_Q (μ s)	E_Q (mJ/cm ²)	$\langle P_{out} \rangle$ (W/m)	P_Q (kW/m)
a	4	19	0.65	737	335
b	10	1	0.19	537	313
c	20	0.5	0.12	675	110

resulting sequence of pulses together with an expanded view. The average electro-optic efficiency is 14.7% for a mean pulse energy of 5 mJ. In any case it is possible in principle to use the resonant properties of an etalon as switching element, if we ignore for the moment the practical impossibility to move the optic at 100 kHz. Moreover, the pulses show a number of undesirable effects:

- irregular peak intensity,
- irregular pulse spacing,
- irregular occurrence of satellite pulses.

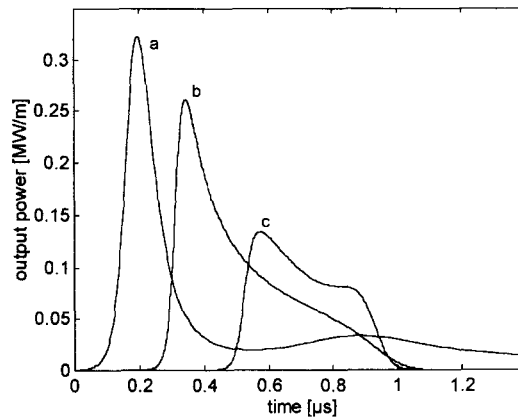


Fig. 14. Q -switched pulse shape as a function of chopping frequency: (a) 4 kHz; (b) 10 kHz; (c) 20 kHz. The curves are horizontally displaced and the time origin moved (to ensure picking a 'steady state' pulse) to facilitate comparison.

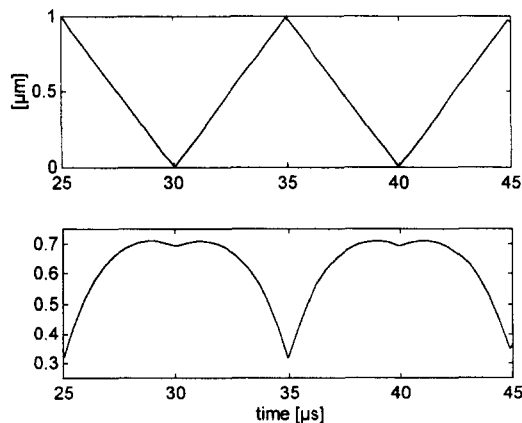


Fig. 15. Upper trace: piezo-driven etalon spacing modulation. Lower trace: resulting reflectivity modulation.

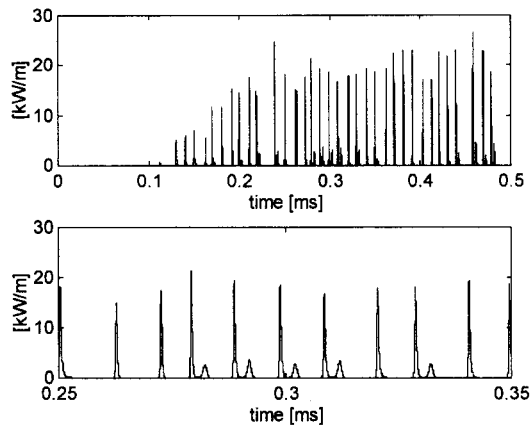


Fig. 16. Q -switched pulse train obtained with the etalon behaving as in Fig. 15. The lower trace shows an expanded view. Note the irregular peak intensity modulation and the occurrence of satellite pulses.

If we limit the spacing modulation frequency to the more realistic value of 500 Hz, we can only reach the short cavity opening time necessary to generate Q -switching if we increase the modulation amplitude, which in turn is practically limited to a few μm (see Fig. 17). Fig. 18 shows the resulting pulse train for an etalon reflectivity depicted in Fig. 17. The pulse energy has increased to $E_Q = 64$ mJ, at an average efficiency of 19% and a peak power of 9 kW/m. The long pulse tail can be explained as follows. When the cavity ‘opens’ it takes a relatively long time for the pulse to build up from spontaneous emission due to the relatively low gain in a CO_2 laser and the delay time involved with the transfer of energy from the nitrogen reservoir. This explains why it is possible to generate giant pulses with relatively long (tens of μs) opening times. When the laser field is established however, the circulating intensity follows the instantaneous value of the cavity Q -factor, with a small delay of the order of the round trip time (tens of ns). As long as the laser is above threshold the shape of the pulse tail will then follow the decreasing reflectivity whose falling edge is determined by Eq. (33). If one is only interested in the ‘purely’ Q -switched giant pulse as in Fig. 12, the etalon seems not to be the appropriate switching element.

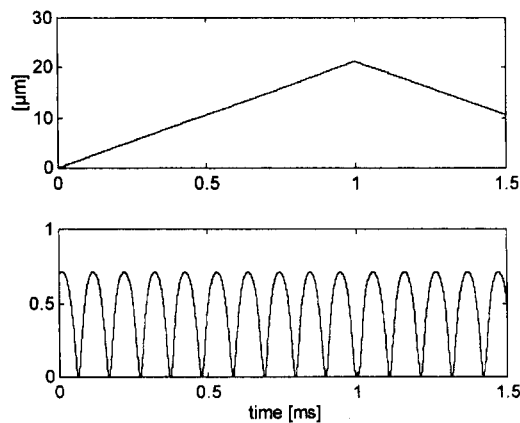


Fig. 17. 500 Hz etalon spacing modulation (upper trace), resulting in a 10 kHz reflectivity modulation (lower trace).

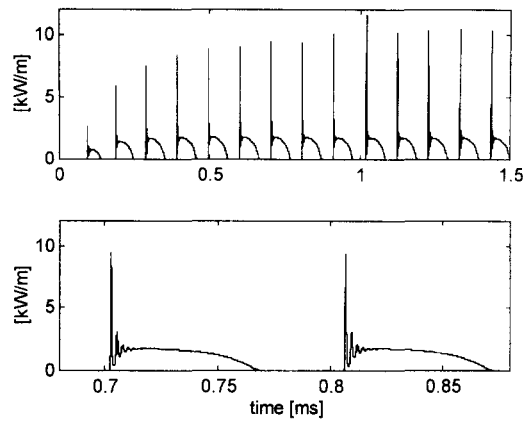


Fig. 18. 10 kHz pulse train obtained with an etalon reflectivity as in Fig. 17.

3.7. Cavity dumping as alternative technique

The dual technique to *Q*-switching is commonly known as *cavity dumping*: the etalon reflectivity is kept at a high value, allowing the intra-cavity laser field to attain a very high intensity, after which the transmission is suddenly switched to nearly 100%. The optical energy stored in the resonator is then released in a pulse with a FWHM of the order of the round trip time.

To attain this kind of behaviour the etalon is equipped with highly reflecting optics, $R = 0.99$, resulting in a reflectivity as shown in Fig. 19 for $d = 2\lambda$ and $f = 600$ Hz. The pulse frequency is 12 kHz for a mean pulse energy of 15.8 mJ. The peak intensity is only 8 kW/m. The output of the laser is depicted in Fig. 20. It is impossible to increase the pulse energy without using unrealistic etalon parameters or creating unwanted effects such as satellite pulses or a strongly varying peak intensity.

The reasons for the problems encountered when using the etalon as switching element are twofold. On the one hand there is the high optimum output coupler reflectivity, which causes the long leading edge of the pulse (Fig. 20, expanded view). On the other hand it should be noted that the factor of influence on the laser dynamics is not the output coupler reflectivity in se, but rather the cavity decay time τ_c . The resonant behaviour of the

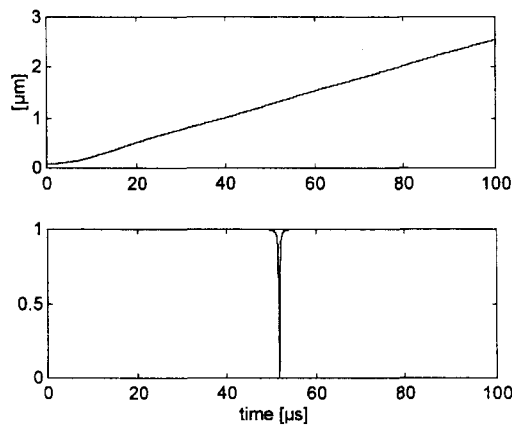


Fig. 19. Resonant behaviour of the etalon reflectivity (lower trace) as a function of etalon spacing (upper trace) when equipped with highly reflecting optics in order to generate cavity dumping.

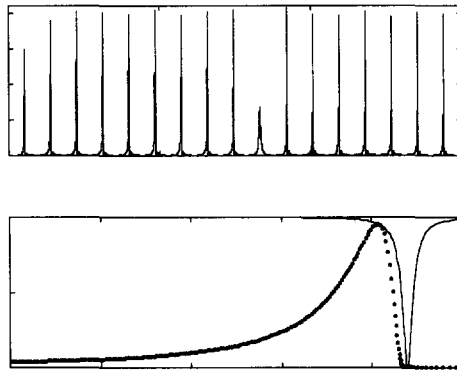


Fig. 20. Upper trace: cavity dumped pulse train. Lower trace: normalized and expanded view of the etalon reflectivity ($R_{\text{et}} = 1 - T_{\text{et}}$; solid curve) and the resulting laser output (dotted curve). Note the long leading edge.

etalon reflectivity (Fig. 19) is strongly broadened by the logarithmic relationship between both quantities (Eq. (12)).

4. Conclusion

The model reported in this paper is concerned with the overall kinetics of the molecular excitation in a fast-flow CO_2 laser. It is not intended to be used for lasing mode analysis, calculation of discharge stability limits and other features of importance to CO_2 laser R&D. However, there is interest in and need for simplified models allowing to quickly assess the influence of the structure of interacting energy reservoirs, inherent to the CO_2 laser, on the modulation behaviour of the laser (it should be noted that solving the complete set of equations over a millisecond time scale takes only some minutes on a Pentium PC, depending on the type of calculation).

The results obtained, ranging from CW lasing to resonator dumping, illustrate the applicability of the model. Computer simulations of laboratory tests on real lasers, in particular relaxation oscillation and Rigrod analysis, yield realistic values of small signal gain, saturation intensity and electro-optic efficiency. The electrical pulsing behaviour, depicted in Fig. 10, will (unfortunately) look very familiar to many a laser engineer. Modulation of the cavity decay rate shows the influence of the overall molecular kinetics on the resulting pulse shape. The long-term behaviour of pulse shape and repeatability (energy, peak power) clearly illustrates the importance of reliably modelling the discharge molecular dynamics over a time scale long enough to incorporate all kinetic processes, in particular the slower, thermal ones.

Acknowledgements

This work was funded by the Flemish Institute for the Advancement of Scientific and Technological Research in Industry, IWT, Brussels, Belgium and frames within Eureka project EU990.

References

- [1] K. Smith, R.M. Thomson, *Computer Modeling of Gas Lasers*, Plenum, New York, 1978.
- [2] S. Sazhin, P. Wild, C. Leys, D. Toebaert, E. Sazhina, The three-temperature model for the fast-axial-flow CO_2 laser, *J. Phys. D* 26 (1993) 1872–1883.

- [3] S. Sazhin, P. Wild, E. Sazhina, M. Makhlof, C. Leys, D. Toebaert, The three-dimensional modelling of processes in the fast-axial-flow CO₂ laser, *J. Phys. D* 27 (1994) 464–469.
- [4] M. Spiridonov, C. Leys, D. Toebaert, S. Sazhin, E. Desoppere, P. Wild, S.M.P. McKenna-Lawlor, Investigation of the active medium of a DC-excited fast-axial-flow CO₂ laser using a tunable diode laser, *J. Phys. D* 27 (1994) 962–969.
- [5] D. Toebaert, P. Muys, E. Desoppere, Spatially resolved measurement of the vibrational temperatures in the plasma of a DC-excited fast-axial-flow CO₂ laser, *IEEE J. Quantum Electron.* 31 (10) (1995) 1774–1778.
- [6] D. Toebaert, P. Muys, E. Desoppere, Vibrational cooling of the active medium of a CO₂ laser by the intra-cavity radiation flux, *J. Phys. D* 29 (7) (1996) 1910–1916.
- [7] M.G. Baeva, P.A. Atanasov, Numerical investigation of CW CO₂ laser with a fast turbulent flow, *J. Phys. D* 26 (1993) 546.
- [8] R.E. Beverly III, Kinetic modelling of a fast-axial-flow CO₂ laser, *Opt. Quantum Electron.* 14 (1982) 25–40.
- [9] R. Rudolph, A. Harendt, P. Bisin, H. Gündel, Numerical modelling of fast-flow CO₂ lasers, *J. Phys. D* 26 (1993) 1872.
- [10] F. Offenhäuser, Theory and experiments on the power modulation of CO₂ lasers, *IEEE J. Quantum Electron.* 24(7) (1988).
- [11] M. Spiridonov, D. Toebaert, E. Desoppere, Diagnostics of a fast-axial-flow CO₂ laser active medium using diode laser spectroscopy techniques, Proc. 11th Symp. School on High Resolution Molecular Spectroscopy, HighRus '93, June 28–July 7, 1993, Moscow-Nizhni Novgorod, Moscow, SPIE 2205.
- [12] G.N. Pearson, D.R. Hall, Vibrational population distributions in RF excited CO laser discharges, *J. Phys. D* 22 (1989) 1102–1106.
- [13] C.E. Treanor, J.W. Rich, R.G. Rehm, Vibrational relaxation of anharmonic oscillators with exchange-dominated collisions, *J. Chem. Phys.* 48 (1968) 1798.
- [14] A. Cenian, Study of nonequilibrium vibrational relaxation of CO₂ molecules during adiabatic expansion in a supersonic nozzle. Treanor type distribution — existence and generation, *Chem. Phys.* 132 (1989) 41–48.
- [15] A.E. Siegman, *Lasers*, University Science Books, California (1986).
- [16] W.L. Morgan, B.M. Penetrante, ELENDF: a time-dependent Boltzmann solver for partially ionized gases, *Comp. Phys. Commun.* 58 (1990) 127.
- [17] J.J. Lowke, A.V. Phelps, B.W. Irwin, Predicted electron transport coefficients and operating characteristics of CO₂-N₂-He laser mixtures, *J. Appl. Phys.* 44 (1973) 4664.
- [18] D.C. Cartwright, S. Trajmar, A. Chutjian, W. Williams, Electron impact excitation of the electronic states of N₂. II: Integral cross sections at incident energies from 10 to 50 eV, *Phys. Rev. A* 16 (1977) 1041.
- [19] C. Leys, Karakterisering van een DC-geëxciteerde axiaal doorstroomde CO₂ laserontlading, Ph.D. dissertation, University Gent, Gent, Belgium (1994).
- [20] R.L. Taylor, S. Bitterman, Survey of vibrational relaxation data for processes important in the CO₂-N₂ laser system, *Rev. Mod. Phys.* 41(1), January 1969.
- [21] W.J. Witteman, *The CO₂ laser*, Springer, Berlin (1987).
- [22] M. Ciofini, R. Meucci, Determination of the effective number of rotational levels affecting the dynamics of CO₂ lasers, *IEEE J. Quantum Electron.* 31(5), 1995.
- [23] W.W. Rigrod, Saturation effects in high-gain lasers, *J. Appl. Phys.* 36 (1965) 2487–2490.
- [24] K. Schindler, G. Staupendahl, Ein neuartiger CO₂ Impulslaser für die Materialbearbeitung, *Jahrbuch LASER* 3, Vulkan, Essen, 1993.